Turkish Journal of Electrical Engineering & Computer Sciences

http://journals.tubitak.gov.tr/elektrik/

Research Article

Turk J Elec Eng & Comp Sci
(2021) 29: 223 – 240

doi:10.3906/elk-2005-75

Speed-sensorless predictive torque controlled induction motor drive with feed-forward control of load torque for electric vehicle applications

Emrah ZERDALİ[1,*], **Rıdvan DEMİR**[2]

[1]Electrical and Electronics Engineering Department, Faculty of Engineering, Niğde Ömer Halisdemir University, Niğde, Turkey

[2]Mechatronics Engineering Department, Faculty of Engineering, Niğde Ömer Halisdemir University, Niğde, Turkey

Received: 12.05.2020 • **Accepted/Published Online:** 30.09.2020 • **Final Version:** 27.01.2021

Abstract: Nowadays, the global trend is towards reducing CO_2 emissions and one solution is to replace internal combustion vehicles with electric vehicles. To this end, electric drive system, the most crucial part of an electric vehicle, has gained importance and has become a major research field. The induction motor (IM) is one of the best candidates for electric vehicle applications due to its advantages such as having simple and robust design, its low cost maintenance requirements and the ability to operate in harsh environments. However, it has a highly nonlinear model with time-varying electrical and mechanical parameters making them difficult to control. Finite control set-predictive torque control (FCS-PTC) is an inherently suitable and a promising control method for the IM because FCS-PTC is easy to implement and has the ability to handle nonlinearities with the inclusion of constraints. In addition, the elimination of speed sensors increases the reliability of electric motor drives while reducing cost and hardware complexity. In this paper, a speed-sensorless FCS-PTC based IM drive system is designed in order to combine the aforementioned advantages. Unlike the current literature, to improve the torque response of conventional FCS-PTC, the load torque is also estimated by an adaptive fading extended Kalman filter and is fed back into the torque control loop. The results show that improved control performance is achieved.

Key words: Induction motor, model predictive control, speed-sensorless control, nonlinear Kalman filtering

1. Introduction

In recent years, there has been a global effort to reduce CO_2 emissions; therefore, renewable and sustainable energy resources and electric vehicles have become the main alternative solutions. With the increase in private and public investment, the drive to develop higher-quality and low-cost alternative products has gained momentum. At this point, the electric drive system, which is one of the most crucial parts of electric vehicle, has become the focus of interest for researchers working in the fields of electrical machines, power electronics, and control systems.

Induction motors (IMs) and permanent magnet synchronous motors are the best options for electric vehicle applications but IMs are more attractive thanks to them being cost-effective. Both motors have a nonlinear model with time-varying electrical and mechanical parameters making them difficult to control. For a long time, their high-performance controls have been carried out by two mature control techniques that have dominated the market: field-oriented control (FOC) and direct torque control (DTC). Compared to FOC, DTC

*Correspondence: ezerdali@ohu.edu.tr

has a simple structure and faster dynamic response as it does not require any modulator and inner current loops [1]. However, DTC has variable switching frequency and high torque ripples that need to be overcome. For this purpose, different approaches based on artificial intelligence, modulator inclusion, and different inverter topologies have been proposed in the literature [2–5], which increase the complexity of DTC. As the complexity of inverter topology increases, control becomes more challenging, and additional control objectives should be considered for high-performance control [6]. Therefore, such a drive system requires the use of more advanced control systems that can handle multivariable systems with nonlinearities and constraints.

At this point, a very promising control method, called model predictive control (MPC), combines the desired advantages, such as dynamic response, easy implementation, and handling nonlinearities with the inclusion of constraints [7, 8]. One of the most preferred MPC strategies in electric drive systems is finite control set-predictive torque control (FCS-PTC). FCS-PTC uses the finite set of possible switching combinations of the inverter and the discretized mathematical model of the system to select the next switching state, which minimizes a predefined cost function. The single cost function, which is the key point of this control strategy, may combine several control objectives, constraints, and nonlinearities [9]. However, Rodriguez et al. [10] state that research efforts in the parameter sensitivity of this strategy, adjustment of the weight factor in the cost function, limitation of the switching frequency, and computational optimization are required to develop more efficient FCS-PTC strategies. For this purpose, some efforts have been made on determining or eliminating the weighting factor [11–13], reducing or fixing the switching frequency [12–15], reducing torque and current harmonics [12, 14–16], overcurrent protection [11, 14–16], minimizing electrical power losses [17], robustness of parameter variation [17, 18], dead time compensation [11, 15, 16, 18], and optimizing computational complexity [12, 14, 16].

On the other hand, eliminating the speed-sensor in electric drive systems, namely speed-sensorless control, reduce cost, hardware complexity, and maintenance requirements while increasing the reliability of the electric drive system. For this purpose, many model-based estimators/observers have been proposed in the literature, such as model reference adaptive systems [19, 20], full-order observers [21, 22], extended Luenberger observers [23, 24], extended and unscented Kalman filters (EKF and UKF) [25–27], and sliding mode observers [28–30]. Unlike the other methods, nonlinear Kalman filtering (NKF) methods (i.e., EKF and UKF) provide a stochastic approach to state/parameter estimation problem by taking into account the process and measurement noises. A very recent study [27] in which EKF and UKF observers are compared for speed-sensorless control applications of IM states that EKF is still the best option with low computational complexity and an estimation performance similar to UKF. However, NKF methods require a stochastic system with complete dynamic and measurement equations to perform optimal estimations, and in many practical applications, those are either unknown or partially known [31]. To overcome this difficulty, different adaptive nonlinear Kalman filtering methods based on multiplemodel, adaptive fading, strong tracking, and innovation, which are capable of compensating for the effect of inaccurate information, have been proposed. A very recent study [32] that compares those methods for real-time speed-sensorless control applications of IM emphasizes that the best option is the adaptive fading based approach considering its simplicity and performance improvement.

In the literature, IM models used in observers can be considered in two main groups: the first group considers the mechanical speed as a fixed state under the assumption infinite inertia hypothesis [33] and the second group takes it into account as a dynamic state with the help of the equation of motion [34]. The second group models improve the speed estimation performance at low speeds due to the inclusion of the mechanical

model. However, it requires load information that is costly and generally impossible to measure. To overcome this problem, the load torque is included as an additional fixed state in the second group models.

Another consideration of this paper is to improve the response of the conventional speed control loop of FCS-PTC and the unknown load-torque has the greatest adverse effect on the speed control loop. To eliminate this effect, disturbance observer (DO) based studies [18, 23] have been proposed in the literature. However, multiple observer designs are needed to perform speed-sensorless control with DO, which leads to an increase in the complexity of the electric drive system.

The main contribution of this paper is to design an FCS-PTC based speed-sensorless IM drive with a feed-forward control (FFC) loop of load torque. The angular speed required for speed control and FCS-PTC algorithm and the flux required for FCS-PTC algorithm are provided by an adaptive fading-based EKF (AFEKF) observer. The AFEKF uses an observer model, which takes place in the second group to estimate the load torque and to improve the estimation performance at low speeds. In addition, by the use of the estimated load torque in the FFC loop, load disturbance rejection is also performed without additional effort. Thus, the conventional torque response of FCS-PTC based IM drive is clearly improved. To reduce the torque ripples, FCS-PTC is fed by the stator currents filtered by the AFEKF. The proposed speed-sensorless electric motor drive system has been tested and verified in simulations under different operating conditions, including speed reversals, load variations, and parameter mismatches.

The rest of this paper is organized as follows: Section 2 derives the mathematical model of IM fed by two level-voltage source inverter (2L-VSI). Section 3 gives the design stages of the AFEKF observer. Section 4 presents speed-sensorless FCS-PTC of IM with FFC. Section 5 demonstrates the effectiveness of the proposed electric drive system. Finally, Section 6 gives the conclusion.

2. Mathematical model of IM fed by 2L-VSI

The IM model in the stator stationary axis can be expressed in the following compact form:

$$\dot{\mathbf{x}}_t = \mathbf{f}(\mathbf{x}_t, \mathbf{u}_t) + \mathbf{w}_t \tag{1a}$$

$$\mathbf{z}_t = \mathbf{h}(\mathbf{x}_t) + \mathbf{v}_t \tag{1b}$$

where $\mathbf{f}$ is the nonlinear function of states and inputs, $\mathbf{h}$ is the function of outputs, $\mathbf{x}_t$ is the state vector, $\mathbf{u}_t$ is the control input vector, $\mathbf{w}_t$ and $\mathbf{v}_t$ are zero-mean Gaussian distributed process and measurement noises, respectively.

Details of vectors in (1) are as follows:

$$\mathbf{x}_t = \begin{bmatrix} i_{s\alpha} & i_{s\beta} & \psi_{r\alpha} & \psi_{r\beta} & \omega_m \end{bmatrix}^T,$$

$$\mathbf{u}_t = \begin{bmatrix} v_{s\alpha} & v_{s\beta} \end{bmatrix}^T, \mathbf{h} = \begin{bmatrix} i_{s\alpha} & i_{s\beta} & \omega_m \end{bmatrix}^T,$$

$$\mathbf{f} = \begin{bmatrix} -\left(\frac{R_s}{L_\sigma} - \frac{R_r L_m^2}{L_\sigma L_r^2}\right) i_{s\alpha} + \frac{R_r L_m}{L_\sigma L_r^2}\psi_{r\alpha} + \frac{L_m p_p}{L_\sigma L_r}\omega_m \psi_{r\beta} + \frac{v_{s\alpha}}{L_\sigma} \\ -\left(\frac{R_s}{L_\sigma} - \frac{R_r L_m^2}{L_\sigma L_r^2}\right) i_{s\beta} + \frac{R_r L_m}{L_\sigma L_r^2}\psi_{r\beta} - \frac{L_m p_p}{L_\sigma L_r}\omega_m \psi_{r\alpha} + \frac{v_{s\beta}}{L_\sigma} \\ \frac{R_r L_m}{L_r} i_{s\alpha} - \frac{R_r}{L_r}\psi_{r\alpha} - p_p \omega_m \psi_{r\beta} \\ \frac{R_r L_m}{L_r} i_{s\beta} - \frac{R_r}{L_r}\psi_{r\beta} + p_p \omega_m \psi_{r\alpha} \\ \frac{3}{2}\frac{p_p}{J_t}\frac{L_m}{L_r}(\psi_{r\alpha} i_{s\beta} - \psi_{r\beta} i_{s\alpha}) - \frac{B_t}{J_t}\omega_m - \frac{\tau_l}{J_t} \end{bmatrix}.$$

where $i_{s\alpha}$ and $i_{s\beta}$ are the stator stationary axis components of stator currents, $\psi_{r\alpha}$ and $\psi_{r\beta}$ are the stator stationary axis components of rotor fluxes, ω_m is the mechanical angular rotor speed, τ_l is the load torque, $v_{s\alpha}$ and $v_{s\beta}$ are the stator stationary axis components of stator voltages, R_s and R_r are the stator and rotor resistances, respectively; L_s and L_r are the stator and rotor inductances, respectively; L_m and $L_\sigma \triangleq \sigma L_s \triangleq L_s - L_m^2/L_r$ are the mutual and leakage inductances, respectively; p_p is the pole-pairs; B_t and J_t are the total viscous friction and inertia of both load and motor, respectively.

A 2L-VSI shown in Figure 1a is used, and the switching state $\vec{S}$ can be defined as

$$\vec{S} = \frac{2}{3}(S_a + \vec{a}S_b + \vec{a}^2 S_c) \tag{2}$$

where $\vec{a} \triangleq e^{j2\pi/3}$ and $S_x \in \{S_a, S_b, S_c\}$ indicate ON/OFF states of upper switches on each leg. The inverter output voltage $\vec{v}_s$ can be expressed by using switching state $\vec{S}$ as follows:

$$\vec{v}_s = V_{\rm dc}\vec{S} \tag{3}$$

where $V_{\rm dc}$ is the dc-link voltage. Considering 2L-VSI, (3) yields seven different voltage vectors, called finite control sets, for eight switching combinations. Those voltage vectors can be seen in Figure 1b.

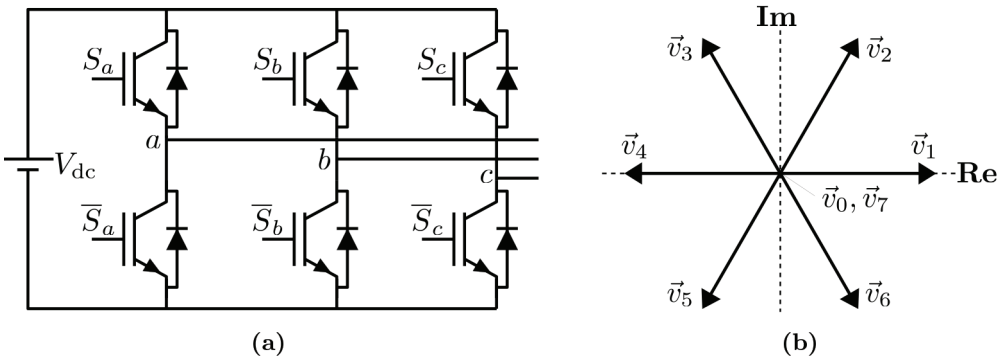

Figure 1. 2L-VSI (a) Circuit topology (b) Possible voltage vectors

3. AFEKF observer

AFEKF observer is the advanced version of the standard EKF with a forgetting (or fading) factor. Zerdali et al. [35] demonstrate that the forgetting factor used in AFEKF clearly improves the estimation performance at transients. Also, the observability analysis of the observer model and the stability analysis of AFEKF were previously performed in [36] and [31], respectively. The AFEKF observer estimates $i_{s\alpha}$, $i_{s\beta}$, $\psi_{r\alpha}$, $\psi_{r\beta}$, and ω_m required for FCS-PTC, ω_m required for speed control, and τ_l required for FFC.

The observer model extended by τ_l can be expressed in the compact form in (1), and the detailed vectors are as follows:

$$\mathbf{x}_{o,t} = \begin{bmatrix} i_{s\alpha} & i_{s\beta} & \psi_{r\alpha} & \psi_{r\beta} & \omega_m & \tau_l \end{bmatrix}^T,$$

$$\mathbf{u}_{o,t} = \begin{bmatrix} v_{s\alpha} & v_{s\beta} \end{bmatrix}^T, \mathbf{h}_o = \begin{bmatrix} i_{s\alpha} & i_{s\beta} \end{bmatrix}^T,$$

$$\mathbf{f}_o = \begin{bmatrix} -\left(\frac{R_s}{L_\sigma} - \frac{R_r L_m^2}{L_\sigma L_r^2}\right) i_{s\alpha} + \frac{R_r L_m}{L_\sigma L_r^2}\psi_{r\alpha} + \frac{L_m p_p}{L_\sigma L_r}\omega_m \psi_{r\beta} + \frac{v_{s\alpha}}{L_\sigma} \\ -\left(\frac{R_s}{L_\sigma} - \frac{R_r L_m^2}{L_\sigma L_r^2}\right) i_{s\beta} + \frac{R_r L_m}{L_\sigma L_r^2}\psi_{r\beta} - \frac{L_m p_p}{L_\sigma L_r}\omega_m \psi_{r\alpha} + \frac{v_{s\beta}}{L_\sigma} \\ \frac{R_r L_m}{L_r} i_{s\alpha} - \frac{R_r}{L_r}\psi_{r\alpha} - p_p \omega_m \psi_{r\beta} \\ \frac{R_r L_m}{L_r} i_{s\beta} - \frac{R_r}{L_r}\psi_{r\beta} + p_p \omega_m \psi_{r\alpha} \\ \frac{3}{2}\frac{p_p}{J_t}\frac{L_m}{L_r}(\psi_{r\alpha} i_{s\beta} - \psi_{r\beta} i_{s\alpha}) - \frac{\tau_L}{J_t} \\ 0 \end{bmatrix}.$$

In the sixth row of the observer model, viscous friction term $B_t\omega_m$ is included in τ_l, that is, the viscous friction term is estimated together with τ_l.

By using the forward Euler approximation

$$\dot{\mathbf{x}}_t \approx \frac{\mathbf{x}_{k+1} - \mathbf{x}_k}{T}, \tag{4}$$

the discretized observer model can be obtained as follows:

$$\mathbf{x}_{k+1} = \mathbf{I}_{6\times 6} \times \mathbf{x}_k + \mathbf{f}_o \times T, \tag{5}$$

where $\mathbf{I}$ is the identity matrix, and T is the sampling time.

The steps of the AFEKF observer are as follows [32, 35]:

1- Definition:

$$\mathbf{F}_{k+1|k} = \left.\frac{\partial \mathbf{f}(\mathbf{x}, \mathbf{u}_k)}{\partial \mathbf{x}}\right|_{\mathbf{x}=\mathbf{x}_k} \tag{6}$$

2- Initialization:

$$\hat{\mathbf{x}}_0 = E[\mathbf{x}_0] \tag{7}$$

$$\mathbf{P}_0 = E\left[(\mathbf{x}_0 - E[\mathbf{x}_0])(\mathbf{x}_0 - E[\mathbf{x}_0])^T\right] \tag{8}$$

3- Time update:

$$\hat{\mathbf{x}}_k^- = \mathbf{f}(\hat{\mathbf{x}}_{k-1}, \mathbf{u}_k) \tag{9}$$

$$\mathbf{P}_k^- = \lambda_k \mathbf{F}_{k|k-1}\mathbf{P}_{k-1}\mathbf{F}_{k|k-1}^T + \mathbf{Q}_{k-1} \tag{10}$$

The optimum fading factor is

$$\lambda_k = \max\left\{1, \frac{tr[\mathbf{N}_k]}{tr[\mathbf{M}_k]}\right\} \tag{11}$$

where $tr[*]$ is the trace of matrix. $\mathbf{N}_k$ and $\mathbf{M}_k$ matrices are

$$\mathbf{M}_k = \mathbf{H}\mathbf{F}_{k|k-1}\mathbf{P}_{k-1}\mathbf{F}_{k|k-1}^T\mathbf{H}^T \tag{12}$$

$$\mathbf{N}_k = \mathbf{C}_0 - \mathbf{R}_k - \mathbf{H}\mathbf{Q}_k\mathbf{H}^T \tag{13}$$

where

$$\mathbf{C}_0 = \begin{cases} \frac{\mathbf{v}_0 \mathbf{v}_0^T}{2}, & k = 0 \\ \frac{[\lambda_k \mathbf{v}_k \mathbf{v}_k^T]}{1+\lambda_k}, & k \geq 1 \end{cases}, \tag{14}$$

$$\mathbf{v}_k = \mathbf{z}_k - \mathbf{H}\hat{\mathbf{x}}_k^-. \tag{15}$$

4- Measurement update:

$$\mathbf{K}_k = \mathbf{P}_k^- \mathbf{H}^T \left[\mathbf{H}\mathbf{P}_k^- \mathbf{H}^T + \mathbf{R}_k\right]^{-1} \tag{16}$$

$$\hat{\mathbf{x}}_k = \hat{\mathbf{x}}_k^- + \mathbf{K}_k \mathbf{v}_k \tag{17}$$

$$\mathbf{P}_k = (\mathbf{I} - \mathbf{K}_k \mathbf{H})\mathbf{P}_k^- \tag{18}$$

where $\mathbf{F}_{k|k-1}$ is the function to linearize the nonlinear model; $\mathbf{P}_k^-$ and $\mathbf{P}_k$ are the priori and the posteriori covariance matrices, respectively; $\mathbf{K}_k$ is the Kalman gain; $\mathbf{Q}_k$ is the covariance matrix of the system noise, namely, modeling errors; $\mathbf{R}_k$ is the covariance matrix of the output noise, namely, measurement noise; $\mathbf{I}$ is the identity matrix.

4. Speed-sensorless FCS-PTC with FFC

The flowchart of the proposed speed-sensorless FCS-PTC of IM with FFC of load torque is presented in Figure 2. The rotor flux required for FCS-PTC and the speed required for FCS-PTC, and speed control are provided by the AFEKF observer. Furthermore, load torque estimation, which improves the speed estimation at low-speeds, is used in the FFC loop to improve the torque response as well.

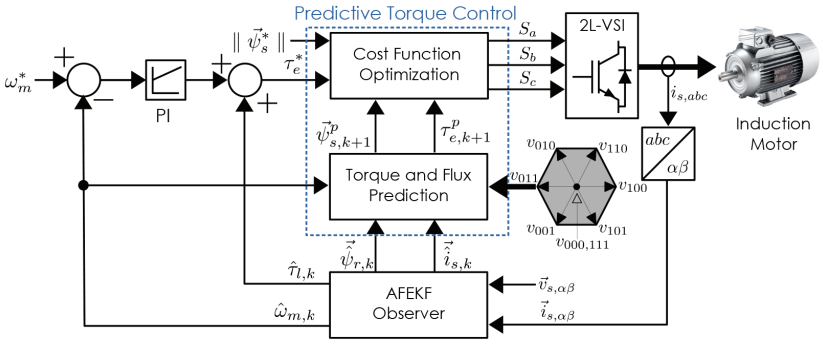

Figure 2. Speed-sensorless FCS-PTC of IM with FFC of load torque.

The stator flux can be derived using the estimated stator current vector $\hat{\vec{i}}_{s,k}$ and rotor flux vector $\hat{\vec{\psi}}_{r,k}$ as follows:

$$\hat{\vec{\psi}}_{s,k} = \frac{L_m}{L_r}\hat{\vec{\psi}}_{r,k} + L_\sigma \hat{\vec{i}}_{s,k} \tag{19}$$

By utilizing $\hat{\vec{i}}_{s,k}$, $\hat{\vec{\psi}}_{r,k}$, and $\hat{\vec{\psi}}_{s,k}$ in the "Torque and Flux Estimation" block, stator fluxes and stator

currents at the time of $k+1$ can be predicted for eight switching combinations as follows:

$$\vec{\psi}^{p\ (j)}_{s,k+1} = \vec{\hat{\psi}}_{s,k} + T\vec{v}^{(j)}_{s,k} - TR_s\vec{\hat{i}}_{s,k},\ j \in \{0,1,\ldots,7\} \tag{20}$$

$$\vec{i}^{p\ (j)}_{s,k+1} = \left(1+\frac{T}{T_\sigma}\right)\vec{\hat{i}}_{s,k} + \frac{T}{T+T_\sigma} \times \left(\frac{1}{R_\sigma}\left(\left(\frac{k_r}{T_r} - k_r j\hat{\omega}_r\right)\vec{\hat{\psi}}_{r,k} + \vec{v}^{(j)}_{s,k}\right)\right),\ j \in \{0,1,\ldots,7\} \tag{21}$$

where $R_\sigma = R_s + k_r^2 R_r$ is the equivalent resistance referred to the stator side, $T_\sigma = L_\sigma/R_\sigma$ is the transient time constant of stator, $T_r = L_r/R_r$ is the rotor time constant, and $k_r = L_m/L_r$ is the rotor coupling factor, $\omega_r = p_p\omega_m$ is the electrical angular rotor speed.

Finally, electromagnetic torques at $k+1$ can be derived for each switching combination as follows:

$$\tau^{p\ (j)}_{e,k+1} = \frac{3}{2}p_p \Im m\left\{(\vec{i}^{p\ (j)}_{s,k+1})(\vec{\psi}^{p\ (j)}_{s,k+1})^*\right\},\ j \in \{0,1,\ldots,7\}. \tag{22}$$

Next, the predicted stator flux vectors and electromagnetic torques, $\vec{\psi}^{p\ (j)}_{s,k+1}$ and $\tau^{p\ (j)}_{e,k+1}$, for eight switching combinations are driven into the "cost function optimization" block. Here, the cost function in (23) is evaluated for all switching combinations, and consequently the optimal voltage vector with the lowest error for both electromagnetic torque and flux is selected for the next switching state.

$$g = \min_{j\in\{0,1,\ldots,7\}}\left(\sum_{h=1}^{N}\left\{\left|\tau^*_e - \tau^{p\ (j)}_{e,k+h}\right| + \lambda_p\left|\left|\vec{\psi}^*_s\right| - |\vec{\psi}^{p\ (j)}_{s,k+h}|\right| + I_{oc,k+h}\right\}\right), \tag{23}$$

where N is the prediction horizon that is accepted one in this study, λ_p is the weighting factor of flux error, I_{oc} is the overcurrent protection term. If the amplitude of the predicted stator current is higher than the allowable current limit ($|i_{s,\max}|$), it activates. Its definition is

$$I_{oc,k+h} = \begin{cases} 0, & \text{if } |\vec{i}^{p}_{s,k+h}| \le |i_{s,\max}| \\ \infty, & \text{if } |\vec{i}^{p}_{s,k+h}| > |i_{s,\max}| \end{cases}. \tag{24}$$

5. Simulation results

Simulation studies are carried out in Matlab Simulink (MathWorks, Inc., Natick, MA, USA) software. In the simulations, a 3 kW, 380 V, 50 Hz, 4-pole, 1430 r/min, 3-phase squirrel-cage type IM with a rated torque of 20 N.m is used, and its rated parameters are given in Table 1. The speed controller is of PI-type. The input voltage vector (i.e., $v_{s,\alpha\beta}$) of the AFEKF observer is derived by using the optimal switching vector $\vec{S}_{\text{opt}}$ and dc-link voltage V_{dc}, as given in (2) and (3).

Table 1. The rated parameters of IM.

R_s [Ω]	R_r [Ω]	L_m [H]	L_s [H]	L_r [H]	B_t [kg.m^2]	J_t [kg.m^2]
2.283	2.133	0.22	0.2311	0.2311	0.001	0.0183

To demonstrate the superiority of the proposed IM drive system, comparative results are presented for the electric drive system with and without FFC loop. To test both electric motor drive systems under different operating conditions, the following scenarios have been determined:

1. The first scenario compares the control performance of both IM drive systems under load torque variations at zero speed.

2. The second scenario demonstrates the control performances under load torque variations at the rated speed.

3. The third scenario illustrates the effect of R_s and R_r variations on the control performances of both IM drive systems. In this test, the effect of L_m variations is ignored since this study does not focus on the field-weakening operation.

4. The fourth scenario shows the performance of the proposed speed-sensorless FCS-PTC based IM drive system for a selected scenario including different operating conditions.

5. In the last scenario, the conventional PI controller is replaced with a fuzzy logic controller (FLC), and the first scenario is repeated again. Thus, the proposed system is tested with a different controller.

In the results shown in Figures 3–10, m and ref superscripts indicate the measured quantities and the reference variations, respectively. $\hat{*}$ shows the quantities estimated by AFEKF observer. Moreover, the mean square error (MSE) values are provided to quantitatively support the results.

In simulations, the sampling time T is 25 μs, excluding Figures 4 and 6. In these figures, the sampling time is 100 μs to demonstrate the performance at lower sampling times. All initial conditions of states in the AFEKF observer are considered as zero. Using trial-and-error method, the proportional (K_p) and integral (K_i) coefficients of the PI controller taking place in the speed control loop have been selected as 10 and 50, respectively. To provide a good control performance at both steady states and transient states, the flux weighting factor, λ_p, in the cost function has been chosen empirically 50. The $\mathbf{Q}$, $\mathbf{R}$, and $\mathbf{P}_0$ matrices used in the AFEKF observer are as follows:

$$\mathbf{Q} = \text{diag}\left\{10^{-4} \quad 10^{-4} \quad 10^{-8} \quad 10^{-8} \quad 10^{-4} \quad 10^{-3}\right\},$$
$$\mathbf{R} = \text{diag}\left\{10^{-4} \quad 10^{-4}\right\},$$
$$\mathbf{P}_0 = \text{diag}\left\{1 \quad 1 \quad 1 \quad 1 \quad 1 \quad 1\right\}.$$

5.1. Scenario-I

In the first scenario, the proposed speed-sensorless FCS-PTC controlled IM drive system is tested under load torque change at zero speed. To show its effectiveness, its performance is compared to that of the same motor drive without FFC of load torque. To this end, the IM is loaded to its rated load at $t = 0.5$ s while it operates at zero speed without load. The resulting control performances can be seen in Figure 3. Although both electric drive systems can overcome the applied load change, the transient state of FCS-PTC with FFC is shorter 92% than that of FCS-PTC without FFC. Furthermore, the estimated currents and fluxes are very close to the measured ones as seen in Figure 3.

In addition, the same scenario is repeated for a sampling time of 100 μs to examine the effect of lower sampling times, and a similar improvement is achieved as shown in Figure 4. Although good control performance has been achieved, it can be observed that ripples increase with decreasing sampling time.

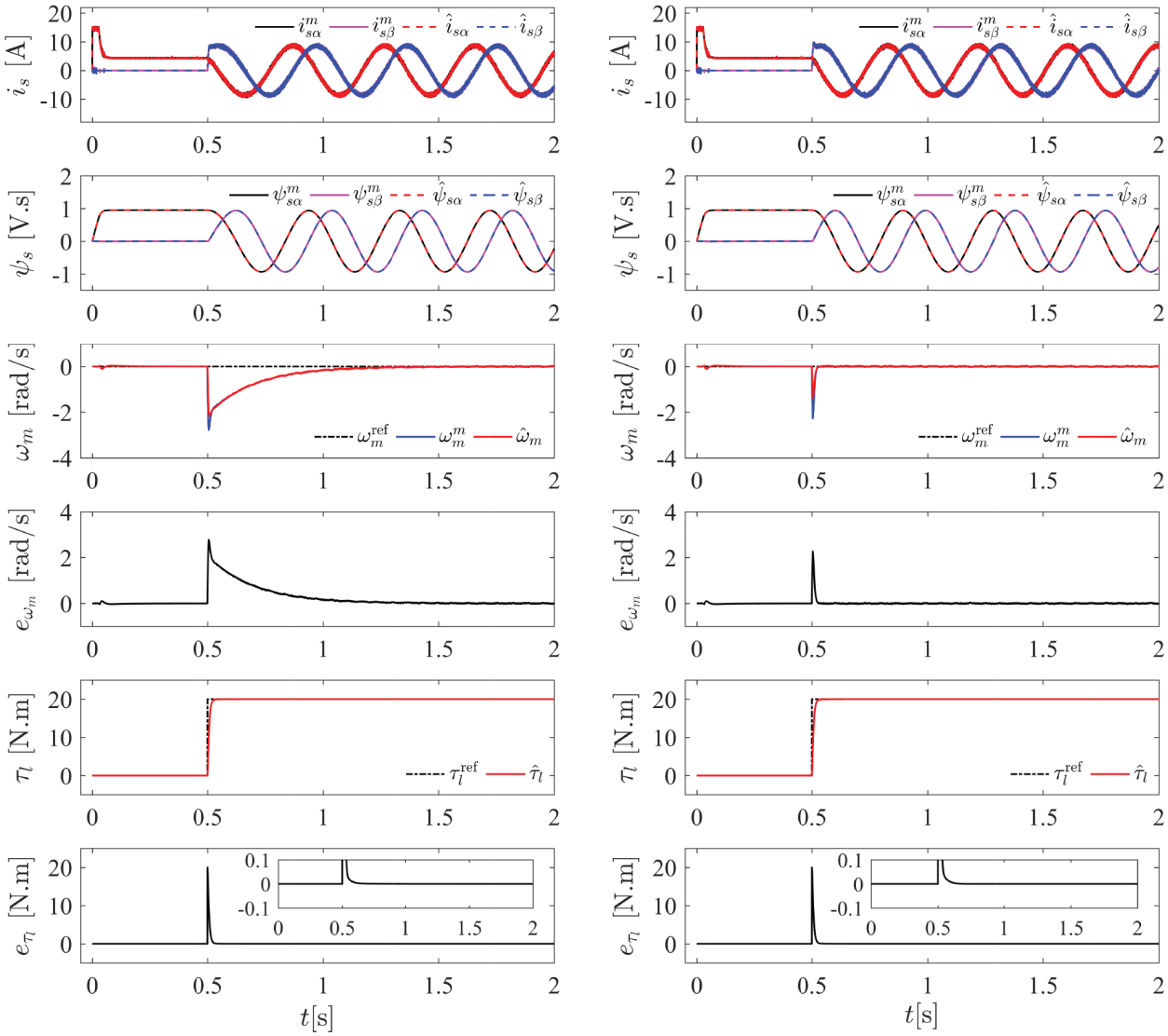

(a) FCS-PTC without FFC **(b)** FCS-PTC with FFC

Figure 3. Zero-speed control performances of both electric drive systems under load change (for $T = 25\ \mu$s)

5.2. Scenario-II

In the second scenario, the proposed IM drive system is tested under the change in load torque at the rated speed. Therefore, the IM is first speeded up to its rated speed, then loaded to the rated load at $t = 0.5$ s. The control performances of both IM drive systems are presented in Figure 5. Similar to the first test, the speed-sensorless FCS-PTC with FFC has a very short transient state compared to that of FCS-PTC without FFC. The constant value in e_{τ_l} at $t = 1.5$ s is not an estimation error. This value corresponds to the viscous

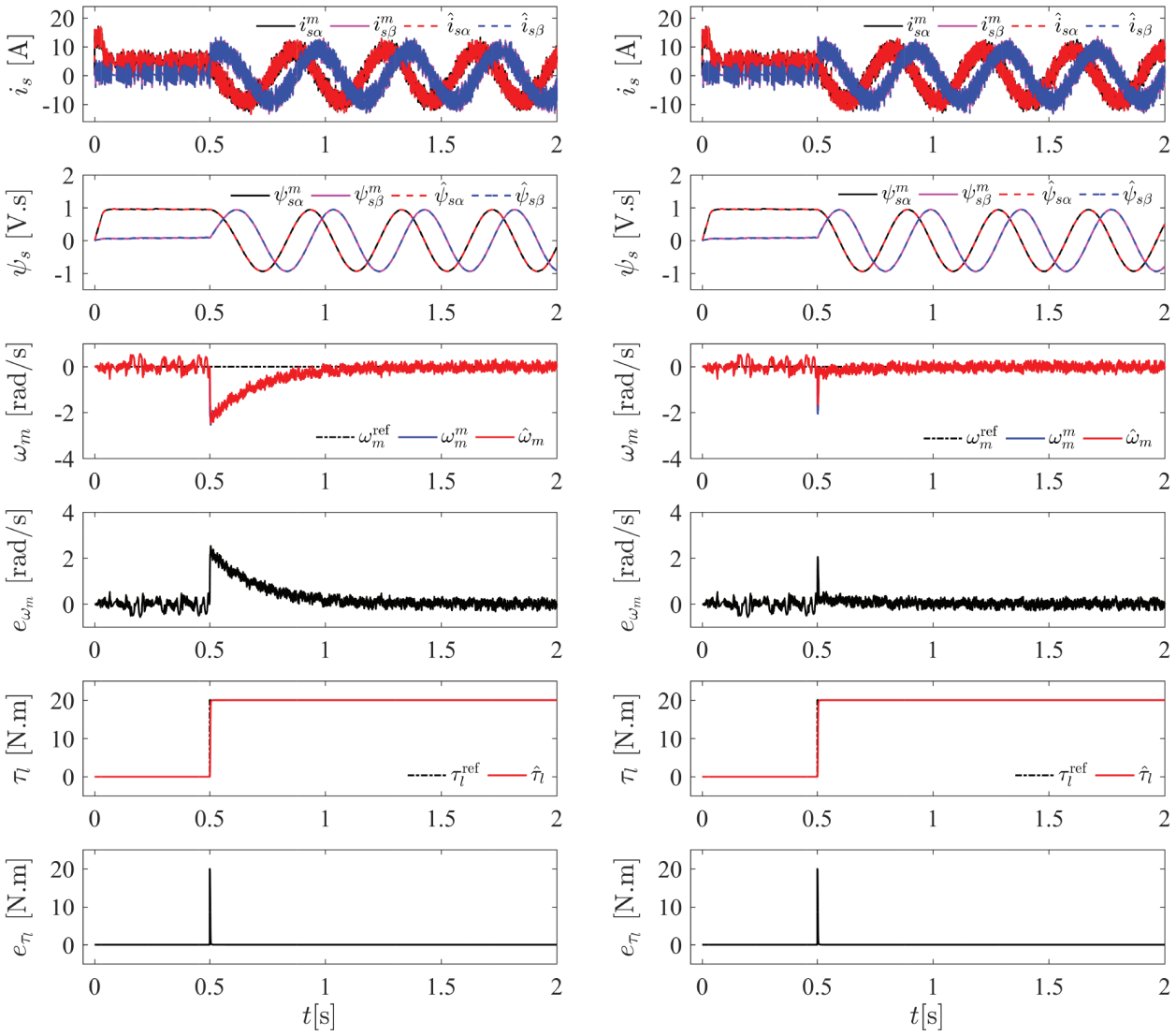

(a) FCS-PTC without FFC **(b)** FCS-PTC with FFC

Figure 4. Zero-speed control performances of both electric drive systems under load change (for $T = 100$ μs).

friction term $B_t\omega_m$ and can be calculated as follows:

$$e_{\tau_l}(1.5) = \tau_l^{\text{ref}} - \hat{\tau}_l = -B_t \times \omega_m(1.5)$$
$$-0.1497 = -0.001 \times 149.7$$
$$-0.1497 = -0.1497$$

This scenario is performed for 100 μs sampling time as well, and the results are shown in Figure 6. A similar improvement has been achieved for lower sampling times with higher fluctuations.

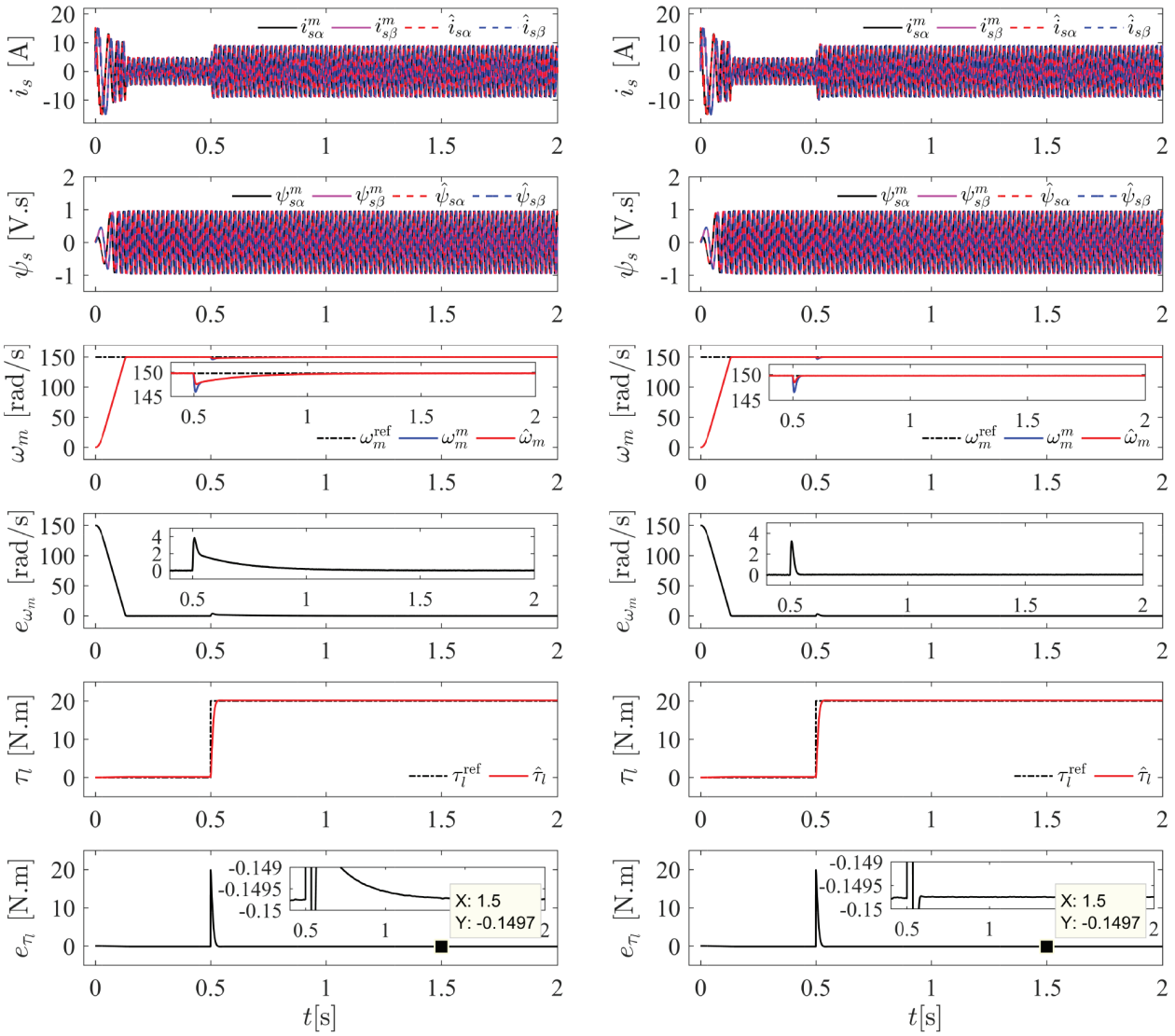

(a) FCS-PTC without FFC **(b)** FCS-PTC with FFC

Figure 5. Control performances of both electric drive systems under load variation at rated speed (for $T = 25\ \mu$s).

5.3. Scenario-III

In the third scenario, the effects of changes in both R_s and R_r on the control performance are studied. The test is carried out at 10 rad/s under the rated load because these variations are more effective at low-speeds under load. To this end, R_s and R_r are increased to 125% of their rated values in the time intervals of $0.6 < t < 1$ s and $1.4 < t < 1.8$ s, respectively. The resulting control performances are presented in Figure 7. As expected, both electric drive systems are sensitive to R_s and R_r changes and their control performances deteriorate in the presence of these variations. To improve the control performance, these changes should be updated in both observer model and FCS-PTC algorithm.

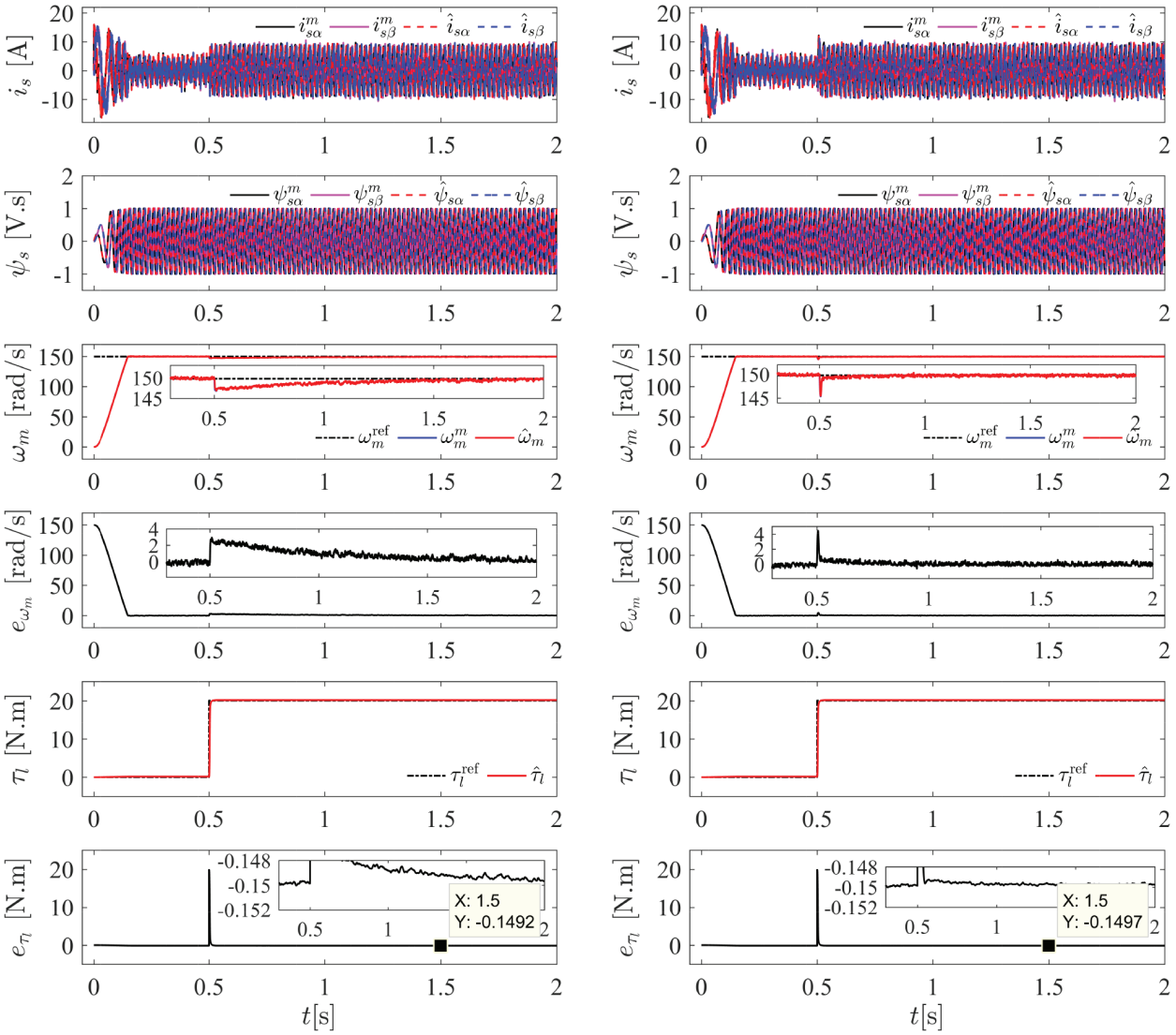

(a) FCS-PTC without FFC **(b)** FCS-PTC with FFC

Figure 6. Control performances of both electric drive systems under load variation at rated speed (for $T = 100\ \mu$s).

5.4. Scenario-IV

In the fourth scenario, the aim is to test the proposed IM drive system in long-term operation under ramp-type speed reference in both directions and step type-load changes. Therefore, a scenario shown in Figure 8 has been determined. The estimation and control performances confirm that the proposed speed-sensorless FCS-PTC based IM drive can operate in both directions under load changes and has satisfactory reference speed tracking capability.

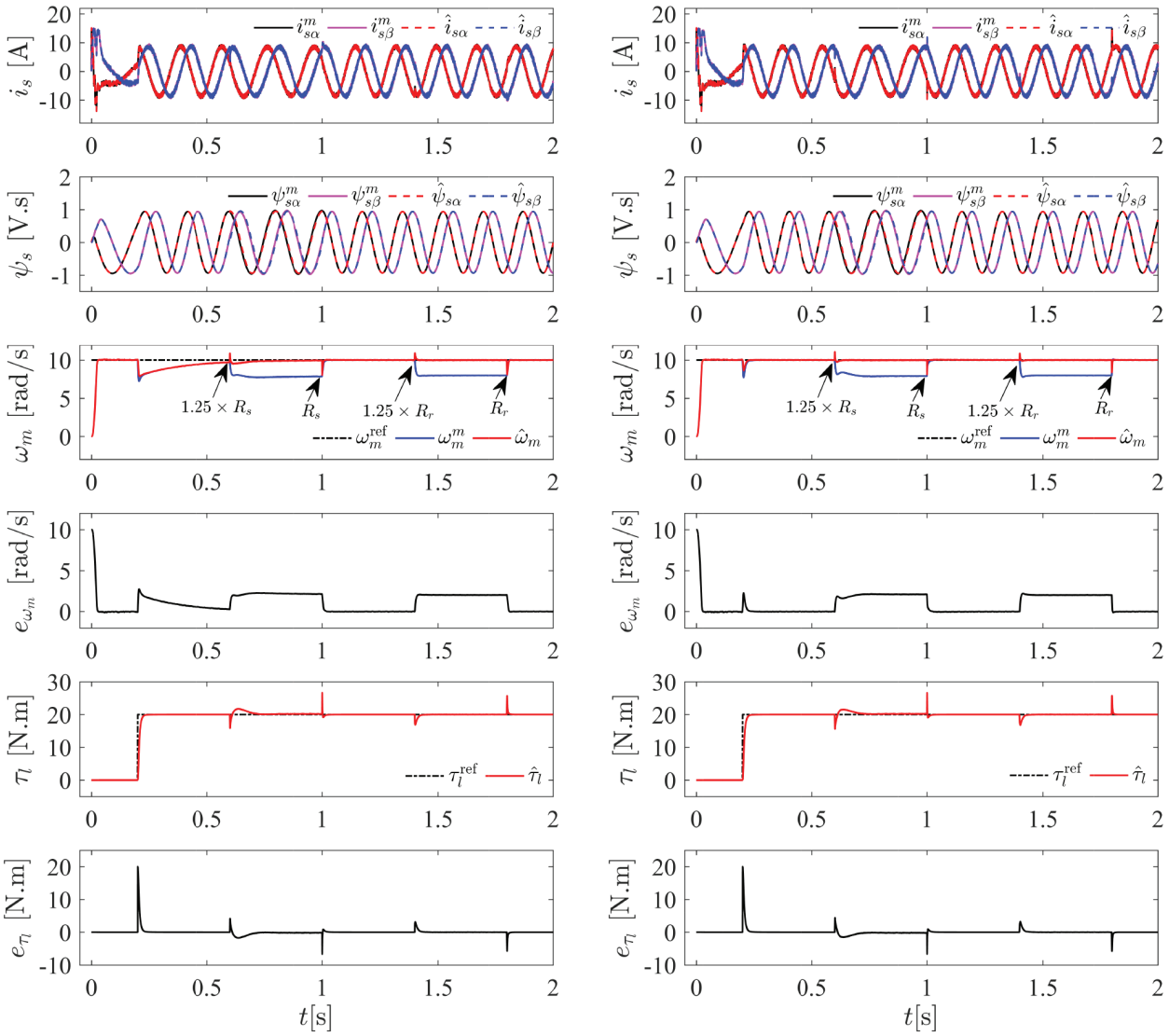

(a) FCS-PTC without FFC **(b)** FCS-PTC with FFC

Figure 7. The effect of R_s and R_r variations on the control performance.

5.5. Scenario-V

In the last scenario, conventional PI controller is replaced with an FLC to test the proposed electric motor drive system with a different controller structure and the new electric motor drive with FLC is tested under the first scenario. The FLC has two inputs (e_ω and Δe_ω) and one output (e_τ). Their membership functions are shown in Figures 9a–9c and each membership function has five linguistic sets: Negative big (NB), negative small (NS), approximately zero (AZ), positive small (PS), and positive big (PB). The structure and rule table for the FLC are presented in Figure 9d and Table 2, respectively. To guarantee the bounds of inputs and limit the output of FLC, saturation blocks have been included in the FLC.

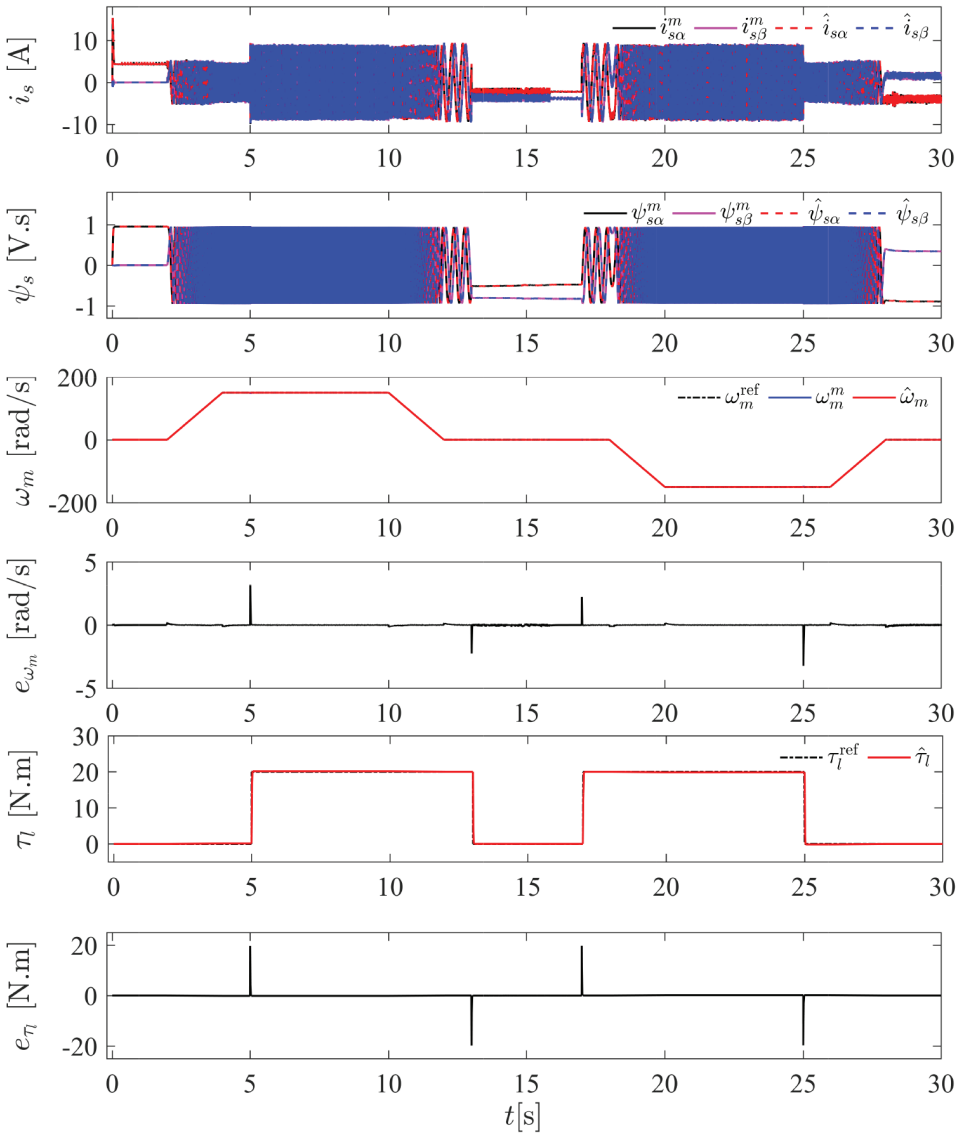

Figure 8. The control performance of the proposed FCS-PTC based IM drive.

Table 2. Rule table for FLC.

Δe_ω \ e_ω	NB	NS	AZ	PS	PB
NB	NB	NB	NS	NS	AZ
NS	NB	NS	NS	AZ	PS
AZ	NS	NS	AZ	PS	PS
PS	NS	AZ	PS	PS	PB
PB	AZ	PS	PS	PB	PB

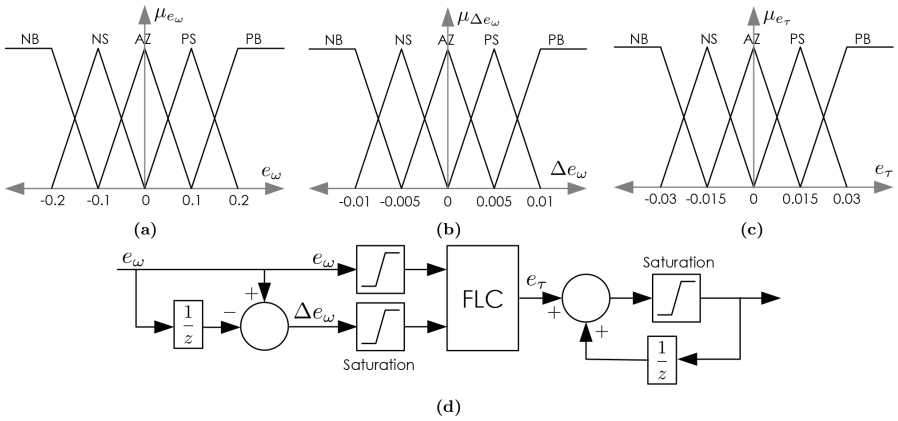

Figure 9. Membership functions and structure of FLC. (a) Membership function of μ_{e_ω}. (b) Membership function of $\mu_{\Delta e_\omega}$. (c) Membership function of μ_{e_τ}. (d) Structure of the designed FLC.

The results for this scenario are shown in Figure 10. In Figure 10a, it can be seen that settling time is greatly reduced compared to the conventional PI controller, but there is an increase in the peak value of speed error. However, it is possible to significantly reduce the peak value by using the FFC of the estimated load torque, as shown in Figure 10b. The relevant MSE values for all scenarios are provided in Table 3.

Table 3. MSE values for Figures 3–10.

	$e_{i_{s\alpha}}$	$e_{i_{s\beta}}$	e_{ω_m}	e_{τ_l}
Figure 3a	0.0219	0.0201	0.2290	0.8281
Figure 3b	0.0212	0.0204	0.0173	0.8269
Figure 4a	0.7674	0.7743	0.2848	0.4333
Figure 4b	0.7569	0.7506	0.0301	0.4330
Figure 5a	0.0154	0.0156	634.9780	1.1172
Figure 5b	0.0154	0.0155	634.6698	1.1188
Figure 6a	0.3818	0.3821	715.9120	0.5209
Figure 6b	0.3724	0.3666	714.3804	0.5205
Figure 7a	0.0227	0.0229	2.6538	1.0081
Figure 7b	0.0230	0.0226	2.3351	1.0104
Figure 8	0.0171	0.0177	0.0105	0.2584
Figure 10a	0.0313	0.0208	1.3181	0.3958
Figure 10b	0.0308	0.0211	0.0297	0.3953

6. Conclusion

In this paper, a speed-sensorless FCS-PTC based IM drive with FFC of the estimated load torque has been designed and has been tested under different operating conditions. The load torque estimation has been used to improve the torque response of FCS-PTC as well as to improve the speed estimation performance of AFEKF observer at low speeds. To show the superiority of the proposed electric motor drive system, its performance has been compared to that of the electric drive without FFC. Also, the conventional PI controller in the speed

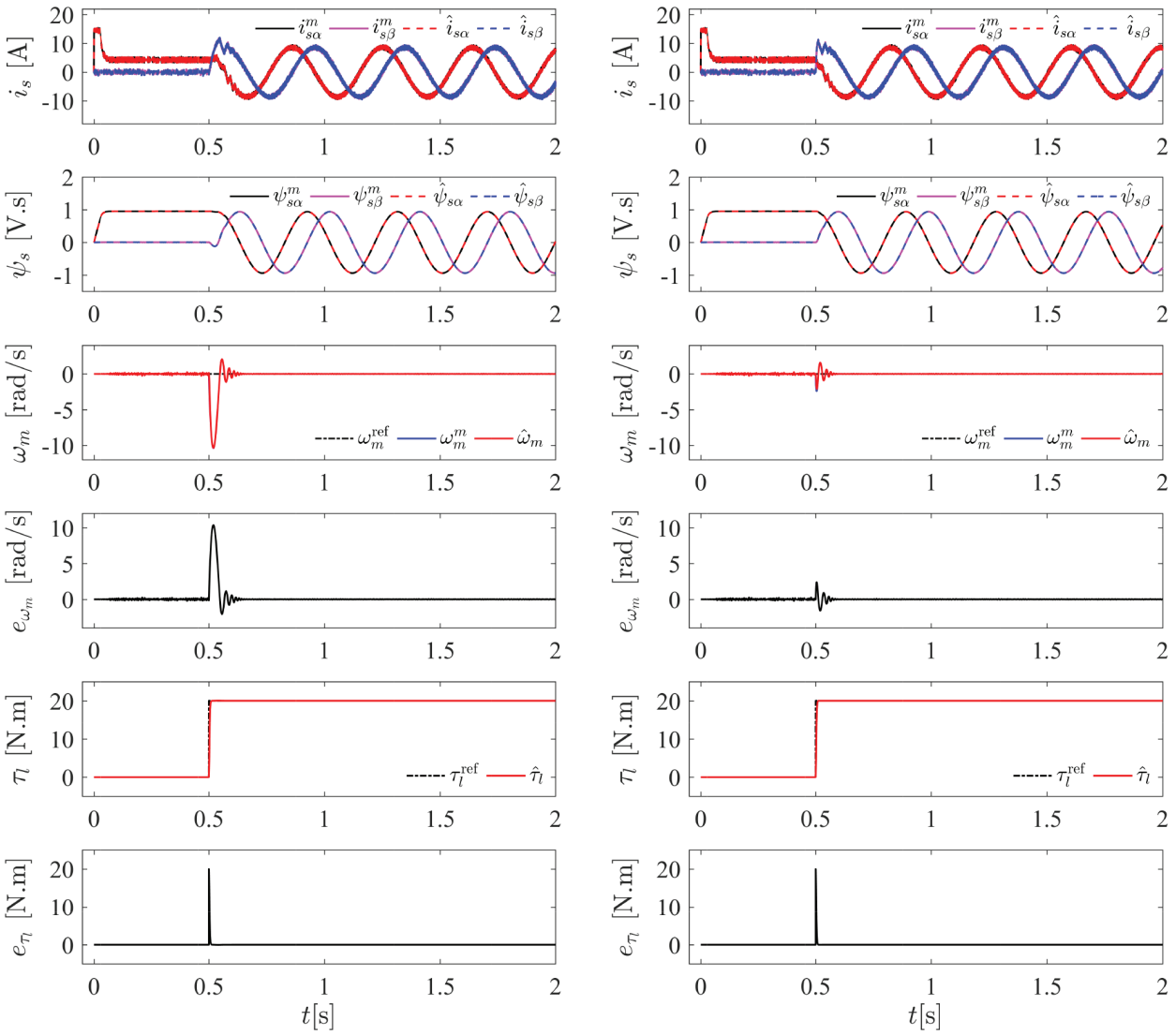

(a) FCS-PTC without FFC **(b)** FCS-PTC with FFC

Figure 10. Zero-speed control performances of both electric drive systems with FLC under load change (for $T = 25\ \mu$s).

control loop has been replaced with an FLC, so that the effect of FFC of the estimated load torque has been demonstrated under different controller structures. Considering the advantages of the proposed IM drive such as the elimination of speed sensors and the ability to reject disturbances such as load torque and viscous friction term, it is suitable for electric drive applications. However, the proposed IM drive system is sensitive to temperature and frequency dependent changes in R_s and R_r; therefore, changes in these parameters need to be updated in both observer model and FCS-PTC algorithm to improve the control performance. Future studies will focus on the solution of this problem.

References

[1] Usta MA, Okumus HI, Kahveci H. A simplified three-level SVM-DTC induction motor drive with speed and stator resistance estimation based on extended Kalman filter. Electrical Engineering 2017; 99: 707-720.

[2] Korkmaz F. Performance improvement of induction motor drives with model-based predictive torque control. Turkish Journal of Electrical Engineering and Computer Science 2020; 28: 525-539.

[3] Alsofyani IM, Idris NRN, Lee K-B. Impact of observability and multi-objective optimization on the performance of extended Kalman filter for DTC of AC machines. Journal of Electrical Engineering & Technology 2019; 14: 231-242.

[4] User Y, Gulez K, Ozen S. Sensorless flux region modification of DTC controlled IM for torque ripple reduction. İstanbul University Journal of Electrical and Electronics Engineering 2014; 14: 1753-1760.

[5] User Y, Gulez K. A new direct torque control algorithm for torque and flux ripple reduction. International Review of Electrical Engineering 2013; 8: 644-653.

[6] Kakosimos P, Abu-Rub H. Predictive speed control with short prediction horizon for permanent magnet synchronous motor drives. IEEE Transactions on Power Electronics 2018; 26: 1623-1637.

[7] Wang F, Zhang Z, Mei X, Rodríguez J, Kennel R. Advanced control strategies of induction machine: Field oriented control, direct torque control and model predictive control. Energies 2018; 11: 120.

[8] Abbasi MA, Husain ARB. Model predictive control of a dual induction motor drive fed by a single voltage source inverter. Turkish Journal of Electrical Engineering and Computer Science 2020; 28: 525-539.

[9] Perez-Guzman RE, Rivera M, Wheeler PW. Recent advances of predictive control in power converters. In: 2020 IEEE International Conference on Industrial Technology (ICIT); 26–28 Feb. 2020; Buenos Aires, Argentina. New York, NY, USA: IEEE. pp. 1100-1105.

[10] Rodríguez J, Kennel RM, Espinoza JR, Trincado M, Silva CA et al. High-performance control strategies for electrical drives: An experimental assessment. IEEE Transactions on Industrial Electronics 2012; 59: 812-820.

[11] Wang F, Xie H, Chen Q, Davari SA, Rodrigues J et al. Parallel predictive torque control for induction machines without weighting factors. IEEE Transactions on Power Electronics 2020; 35: 1779-1788.

[12] V Praveen Kumar K, Kumar TV. Enhanced direct torque control and predictive torque control strategies of an open-End winding induction motor drive to eliminate common-mode voltage and weighting factors. IET Power Electronics 2019; 12: 1986-1997.

[13] Guazzelli PR, de Andrade Pereira WC, de Oliveira CMR, de Castro AG, de Aguiar ML. Weighting factors optimization of predictive torque control of induction motor by multiobjective genetic algorithm. IEEE Transactions on Power Electronics 2019; 34: 6628-6638.

[14] Zhang Y, Yuning B, Yang H, Zhang B. Low switching frequency model predictive control of three-level inverter-fed IM drives with speed-sensorless and field-weakening operations. IEEE Transactions on Industrial Electronics 2019; 66: 4262-4272.

[15] Habibullah MD, Lu DD-C, Rahman MF. Finite-state predictive torque control of induction motor supplied from a three-level NPC voltage source inverter. IEEE Transactions on Power Electronics 2017; 32: 479-489.

[16] Habibullah MD, Lu DD-C, Xiao D, Fletcher JE, Rahman MF. Predictive torque control of induction motor sensorless drive fed by a 3L-NPC inverter. IEEE Transactions on Industrial Informatics 2017; 13: 60-70.

[17] Eftekhari SR, Davari SA, Naderi P, Garcia C, Rodriguez J. Robust Loss minimization for predictive direct torque and flux control of an induction motor with electrical circuit model. IEEE Transactions on Power Electronics 2020; 35: 5417-5426.

[18] Wang J, Wang F, Zhang Z, Li S, Rodriguez J. Design and implementation of disturbance compensation-based enhanced robust finite control set predictive torque control for induction motor systems. IEEE Transactions on Industrial Informatics 2017; 13: 2645-2656.

[19] Korzonek M, Tarchala G, Orlowska-Kowalska T. A review on MRAS-type speed estimators for reliable and efficient induction motor drives. ISA Transactions 2019; 93: 1-13.

[20] Zerdali E, Menguc EC. Novel complex-valued stator current-based MRAS estimators with different adaptation mechanisms. IEEE Transactions on Instrumentation and Measurement 2019; 68: 3793-3795.

[21] Orlowska-Kowalska T, Korzonek M, Tarchala G. Stability improvement methods of the adaptive full-order observer for sensorless induction motor drive – comparative study. IEEE Transactions on Industrial Informatics 2019; 15: 6114-6126.

[22] Yin S, Huang Y, Xue Y, Meng D, Wang C et al. Improved full-order adaptive observer for sensorless induction motor control in railway traction systems under low-switching frequency. IEEE Journal of Emerging and Selected Topics in Power Electronics 2019; 7: 2333 - 2345.

[23] Krishna M, Daya F. Adaptive speed observer with disturbance torque compensation for sensorless induction motor drives using RT-Lab, Turkish Journal of Electrical Engineering and Computer Science 2016; 24: 3792-3806.

[24] Lee K-B, Blaabjerg F. Reduced-order extended luenberger observer based sensorless vector control driven by matrix converter with nonlinearity compensation. IEEE Transactions on Industrial Electronics 2006; 53: 66-75.

[25] Inan R, Barut M. Bi input-extended Kalman filter-based speed-sensorless control of an induction machine capable of working in the field-weakening region. Turkish Journal of Electrical Engineering and Computer Science 2014; 22: 588-604.

[26] Zerdali E, Barut M. Novel version of bi input-extended Kalman filter for speed-sensorless control of induction motors with estimations of rotor and stator resistances, load torque, and inertia. Turkish Journal of Electrical Engineering and Computer Science 2016; 24: 4525-4544.

[27] Yildiz R, Barut M, and Zerdali E. A comprehensive comparison of extended and unscented Kalman filters for speed-sensorless control applications of induction motors. IEEE Transactions on Industrial Informatics 2020; 16: 6423-6432.

[28] Zhang Y, Yin Z, Zhang Y, Liu J. A novel sliding mode observer with optimized constant rate reaching law for sensorless control of induction motor. IEEE Transactions on Industrial Electronics 2020; 67: 5867-5878.

[29] Zaky MS, Metwaly MK, Azazi HZ, Deraz SA. A new adaptive SMO for speed estimation of sensorless induction motor drives at zero and very low frequencies. IEEE Transactions on Industrial Electronics 2018; 65: 6901-6911.

[30] Davari SA, Khaburi DA, Wang F, Kennel R. Robust sensorless predictive control of induction motors with sliding mode voltage model observer. Turkish Journal of Electrical Engineering and Computer Science 2013; 21: 1539-1552.

[31] Kim KH, Jee GI, Park CG, Lee JG. The stability analysis of the adaptive fading extended Kalman filter using the innovation covariance. International Journal of Control, Automation and Systems 2009; 7: 49–56.

[32] Zerdali E. A comparative study on adaptive EKF observers for state and parameter estimation of induction motor. IEEE Transactions on Energy Conversion 2020; 35: 1443–1452.

[33] Bolognani S, Oboe R, Zigliotto M. Sensorless full-digital pmsm drive with ekf estimation of speed and rotor position. IEEE Transactions on Industrial Electronics 1999; 46: 184-191.

[34] Barut M, Bogosyan S, Gokasan M. Speed-sensorless estimation for induction motors using extended kalman filters. IEEE Transactions on Industrial Electronics 2007; 54: 272-280.

[35] Zerdali E, Yildiz R, Inan R, Demir R, Barut M. Adaptive fading extended Kalman filter based speed-sensorless induction motor drive. In: IEEE 2018 XIII International Conference on Electrical Machines (ICEM); Alexandroupoli, Greece. New York, NY, USA; 2018. pp. 1367-1373.

[36] Alonge F, Cangemi T, D'Ippolito F, Sferlazza A. Convergence analysis of extended Kalman filter for sensorless control of induction motor. IEEE Transactions on Industrial Electronics 2015; 62: 2341-2352.